Published in final edited form as:
Magn Reson Med. 2008 September ; 60(3): 575–581. doi:10.1002/mrm.21641.

High spectral and spatial resolution MRI of age related changes in murine prostate

Sean Foxley[1], **Xiaobing Fan**[1], **Sanaz A. Jansen**[1], **Marta Zamora**[1], **Erica Markiewicz**[1], **Hikmat Al-Ahmadie**[2], and **Gregory S. Karczmar**[1,*]

[1]Department of Radiology, University of Chicago, Chicago, IL 60637

[2]Department of Pathology, University of Chicago, Chicago, IL 60637

Abstract

The purpose of this work was to evaluate high resolution echo-planar spectroscopic magnetic resonance imaging of normal and pre-cancerous prostatic changes in a transgenic mouse line. Simian virus large T-antigen transgenic male mice (n = 7, age = 34 ± 3.7 weeks) with prostatic hyperplasia and intraepithelial neoplasia (PIN) were studied. High spectral and spatial resolution (HiSS) MRI of the water proton signal was compared to the FID integral image and conventional gradient echo and spin echo imaging. Water peak-height images of the prostate produced from HiSS datasets showed improved contrast-to-noise ratio ($p < 0.03$), and greater morphological detail ($p < 0.004$) based on texture analysis. Despite the high spectral resolution of the HiSS datasets, signal-to-noise ratio compared favorably with that of the FID integral and conventional images. Lobular features in HiSS images of older mice were consistent with hyperplasia seen on histology. A partially deuterated water-filled catheter was inserted in the mouse rectum for susceptibility matching between the colon interior and exterior to minimize image artifacts. These preliminary results suggest that HiSS MRI provides detailed morphology of the murine prostate and can detect early changes associated with the development of cancer. HiSS MRI of patients may have similar advantages.

Keywords

Prostate; transgenic-mice; EPSI; prostatic hyperplasia; prostate cancer

Introduction

Prostate cancer is the most frequently diagnosed cancer in men in the US, and the second leading cause of cancer-related death for this demographic (1). It is currently recommended by the American Urological Association and the American cancer Society that normal risk men 50 and over receive annual serum prostate specific antigen (PSA) screenings as well as digital rectal exams (1,2). While PSA screening is the current preferred method for early detection, its efficacy still remains in doubt (3). Current long term studies have yet to

*Address Correspondence To: Gregory Karczmar, Ph.D., Professor, Department of Radiology, MC2026, University of Chicago, 5841 S. Maryland Ave., Chicago, IL, USA 60637, Phone: 773-702-0214, Fax: 773-702-1161, gskarczm@uchicago.edu.

demonstrate that it provides a clinically significant survival advantage for men (4,5). Use of PSA screening for early detection is limited by both false positives and false negatives (6).

Prostate imaging is a complimentary procedure to the PSA screening that could aid in rectifying these difficulties. Specifically, MRI provides excellent prostate images due to its strong soft tissue contrast (7). It has been shown to have greater sensitivity for the detection of prostate cancer than both digital rectal exams and transrectal ultrasound (8,9). In light of these findings, much work has been performed to validate and improve its performance. Protocols utilizing various combinations of T_2 weighted, dynamic contrast enhanced, and diffusion weighted imaging have been developed and reported. These studies have yielded mixed results. High histological variability of benign prostate hyperplasia has been suggested as a possible reason for its inconsistent presentation in MR images (10). This inconsistency could limit MR's ability to distinguish between benign prostate hyperplasia and prostatic adenocarcinomas (11-13). Detection rate of prostate cancer in medium and high-risk groups is significantly improved with use of endorectal coils (14). However, even with this improvement in signal detection, conventional imaging techniques still suffer from insufficient sensitivities and low negative predictive values (15). The addition of spectroscopic imaging to detect metabolic markers for cancer has potential applications for guiding therapy, but it has been reported to provide no statistically significant change in diagnostic accuracy when performed in conjunction with MRI (16).

Because of the limited sensitivity and specificity of conventional MRI of the prostate, we proposed the use of high spectral and spatial imaging (HiSS) to provide increased anatomic and functional detail (17-19). In conventional MRI, images are produced from a single point on the proton free induction decay. In high spectral and spatial resolution imaging, the entire proton free induction decay is sampled using chemical shift imaging (20), including echo-planar spectroscopic imaging (21), and related methods. If the proton spectrum in each voxel is a single, smooth Lorentzian line, then fits of the time domain data (i.e. the FID) can produce T_2* maps that provide excellent contrast. However the proton signal *in vivo* often contains significant contributions from water and fat. In addition, the water spectrum from each voxel is often shifted and/or inhomogeneously broadened due to local, subvoxelar variations in magnetic susceptibility (22-28). Therefore, it is advantageous to analyze the complicated proton signal from each voxel in the spectral domain, so that individual Fourier components of the water and fat resonances can be used to produce images (29). B_0 maps derived from the resonance frequency of the peak of the water and fat resonances provide additional information. In conventional images, chemical shift artifacts from fat and consequent spectrally inhomogeneous broadening of the water resonance produce artifacts and degrade image quality (30). In images produced from the individual Fourier components of the water and fat resonances (including the water signal peak height), these artifacts are minimized, and local variations in magnetic susceptibility and chemical shift become a source of increased image contrast and information.

Past work has in this lab has demonstrated that echo-planar spectroscopic imaging (EPSI) of the water and fat proton resonance at high spectral/spatial resolution (HiSS) can increase contrast-to noise ratios (CNR) and while maintaining excellent signal-to-noise ratio (SNR) compared with gradient echo and spin echo images (31,32). Specifically, Du *et al* (32)

demonstrated advantages of water peak height images, produced from the peak amplitude of the water spectrum in each voxel, of mouse prostate tumors inoculated in the hind legs of male rats. Du et al also reported (32) qualitative improvements in HiSS water peak-height images of prostate cancer xenografts orthotopically implanted in Copenhagen rats. However, surgical implantation of tumor tissue is a highly invasive model and implanted tumors were very large. Other work demonstrated that HiSS water peak height images show *in vivo* anatomy with greater morphological detail than conventional MRI in rodent mammary tumors, rodent brain, and human breast (17,33,34). HiSS provides increased fat suppression in MR images of human breast (35,36) compared to conventional non-spectroscopic imaging techniques.

In the work described here, we evaluate HiSS MRI of orthotopic, spontaneously occurring rodent prostate cancer. Because of the importance of clinical MRI of the prostate, pre-clinical models of prostate cancer have been used to aid development and testing of improved MRI methods. Recent pre-clinical research has focused on using transgenic mouse models for imaging prostate cancer with MRI (37-40). For example, Degrassi *et al* report the ability to discriminate between poorly and well differentiated adenocarcinomas in prostates of transgenic mice [simian virus 40 (SV 40) large tumor antigen (TAg) type] that have high rates of prostate cancer (40). Fricke *et al* report the use of a T_1 weighted turbo RARE 3D pulse sequence at 7 T to determine the prostate volume of transgenic mice with promising results (39). While these studies provided valuable information, they focused on well defined advanced tumors (sizes ranging from 1.5 mm – 10+ mm) and the imaging methods were very similar to standard clinical methods.

In the present research, normal prostate and pre-cancerous changes in a transgenic line of male mice [Simian virus large T-antigen (SV40 TAg) type] were imaged. These mice have a recombinant gene expressing simian virus 40 early-region transforming sequences under the regulatory control of the rat prostatic steroid binding protein [C3(1)] gene (41). They develop prostatic hyperplasia early in life that progresses to adenoma or carcinoma in many animals after 7 months. This transgenic model is advantageous compared to other models, such as invasive xenografting of prostate tumor tissue that can distort and/or damage the normal anatomy, because adenocarcinomas developed are spontaneously occurring and are similar to the more poorly differentiated variants of human prostate carcinoma (42).

Artifacts associated with magnetic susceptibility differences between air in the mouse colon and the surrounding tissue were minimized with a partially deuterated water filled catheter inserted in each mouse’s rectum. The quality of conventional gradient and spin echo images were compared with water peak height images derived from HiSS datasets by calculating the signal-to-noise and contrast-to-noise ratios as well as performing texture analysis in the manually segmented prostate. In addition, images derived from spectral data were compared with images derived from time domain data, i.e. FID data. The mean area of the prostate in a single slice from each experiment was measured to track the growth of normal prostate. Histology was qualitatively compared with MRI to characterize the prostate and abnormal prostate growth.

In this work, images produced with HiSS MRI are compared with to single gradient echo and spin echo images. While more sophisticated imaging methods may produce different and/or improved contrast, the comparison reported here was made to evaluate if contrast in HiSS images was qualitatively different from images produced from the most routinely used conventional acquisition techniques. T_2*/T_1 weighted gradient echo images are the conventional equivalent to the water peak height image produced from HiSS datasets, so this comparison was of particular interest.

Materials and Methods

Data Collection

Mouse prostate images were collected at 4.7 T using a Bruker BioSpec 33 cm horizontal bore scanner (Billerica, MA) with 20 cm bore self-shielded gradient coils (maximum gradient strength 100 mT/m). Experiments (n = 7) were performed using mice at 29 to 38 weeks of age (3 mice were 30.3 ± 2.3 weeks; the other 4 were 36.8 ± 1.0 weeks). After the prostate was localized using a series of consecutive multi-slice, low-resolution gradient echo images [TR/TE = 675/25 ms, array size = 128 × 128, field of view (FOV) = 30 mm, in-plane resolution = 234 μm, slice thickness = 1.00 mm, flip angle = 30°, number of averages (NEX) = 2], 'Fastmap' (43) was performed on a ~1 cm^3 voxel centered about the prostate to improve localized shimming to the second order. All imaging was respiratory-gated and collected with a small specialized home-built low-pass birdcage coil designed for mouse abdominal imaging (coil was an 8 leg, cylindrical design with a length and diameter of 3.2 cm each). In order to easily compare images acquired with different pulse sequences, images were acquired at the same slice location with the same spatial resolution. Gradient echo and spin echo images were collected from a single slice per experiment with 117 μm in-plane resolution over a 30 mm field of view and 0.5 mm slice thickness. HiSS data was collected from the same slice, with the same spatial resolution, and with 3.1 Hz spectral resolution. Because all imaging was respiratory gated the minimum TR was determined by the respiration rate of the specific mouse; this was typically ~1200 ms (Gradient echo: TR/ TE = 1100-1300/25 ms, array size = 256 × 256, flip angle = 30°, NEX = 2, receiver bandwidth = 50 kHz. Spin echo: TR/TE = 2000-3000/40 ms, array size = 256 × 256, NEX = 2, receiver bandwidth = 50 kHz. EPSI: TR = 1100-1300 ms, echo spacing = 5.12 ms, array size = 256 × 256 × 64, flip angle = 30°, NEX = 2, receiver bandwidth = 50 kHz). Note that while the acronym EPSI (or CSI when conventional spectroscopic imaging is employed instead) can be used to describe the spectral/spatial imaging protocol, the acronym HiSS is used here to specify that the data is acquired with high special and spectral resolution, and to differentiate this type of imaging from the more common, low resolution spectroscopic imaging of metabolites. The current approach could also be described as spectroscopic micro-imaging.

The spectral bandwidth of the resultant 3D HiSS dataset is ~195 Hz. Data collection timing was defined such that, after spectral aliasing, the fat peak was half the spectral bandwidth from the water peak. This ensured that the water and fat lines were separated for optimal discrimination.

All procedures performed on animals followed protocols approved by the Institutional Animal Care and Use Committee and were in compliance with the Animal Welfare Act and

NIH Guide for the Care and Use of Laboratory Animals. Mice were immobilized on a plexiglas board with vet wrap and tape and anesthetized with 1.5-2 % Isoflurane gas mixed with medical air (2 L/min) delivered through a mask. Temperature, ECG, and respiration rate were continuously monitored throughout each experiment (SA Instruments, Stony Brook, NY). Temperature was maintained using a warm air blower fed into the bore of the magnet.

To minimize blooming artifact around the colon in the images caused by air, a catheter filled with partially deuterated water was inserted in the rectum. This served to closely match the magnetic susceptibility between the interior of the colon and the surrounding tissue. The addition of deuterated water insured that the signal from water in the catheter did not overwhelm signal from the prostate.

Data analysis

Data was processed and analyzed using IDL (RSI, Boulder, CO). EPSI utilizes conventional excitation (in this study, gradient echo) followed by an oscillating, multi-lobed readout gradient train (20). This allows detection of the proton free induction decay (FID) as a function of time for each point in k-space. For the resultant HiSS dataset, each slice of complex raw data was reformatted into a three dimensional array ($k_x \times k_y \times time$).

In cases where the water signal is a single, decaying exponential (producing a pure Lorentzian spectrum after the Fourier transform along the time dimension) the data can be efficiently and accurately analyzed in the time domain to produce a T2* map. However, the proton signal *in vivo* has significant contributions from both water and fat, and in addition, the water spectrum is often inhomogeneously broadened, with asymmetric shoulders and partially resolved components (17). As a result, it is advantageous to analyze the data in the spectral domain. Therefore, 3D arrays were Fourier transformed in all three dimensions to produce two spatial and one spectral dimension ($x \times y \times \nu$). A modulus water spectrum was produced for each image voxel. Spectral ghosting was removed by correcting both the misalignment and error in phase between the even and odd echoes (44) of the gradient echo train. Specifically, these errors are corrected by shifting the center of mass of the even and odd echoes to account for misalignment, followed by a zero-order phase correction applied to the odd echoes to minimize the intensity of spectral ghosts. Improved estimates of the frequency of the water peak were obtained with a frequency shifting method (34) and the spectral intensity baseline for each spectrum was estimated and subtracted (28). The amplitude of the water resonance is proportional to T_2* and inversely proportional to T_1. However, because the TR with respiratory gating is on the order of 1200 ms, the peak height images are often referred to as being strongly T_2* weighted.

A second type of image was produced from the time domain data by Fourier transforming the raw 3D *k-space/time* HiSS dataset over the 2 k-space dimensions. The modulus of the complex 3D dataset was performed, producing a 3D dataset composed of a series of gradient echo images (the number of gradient echo images is equal to the number of lobes in the EPSI gradient echo train) with increasing TE. The sum of all gradient echoes in each HiSS dataset, sometimes referred to as a ‘collapsed’ image, which is the equivalent to integrating the FID for each point in space, was produced (45).

SNR, CNR, and image texture were calculated over the segmented prostate ROI for each experiment; this was performed for all four image types. The prostate was identified by a urologist. An ROI segmenting the prostate was manually selected for each experiment. The SNR was defined as the mean signal over the prostate ROI divided by the standard deviation of the noise. CNR was defined as the difference of the SNR in a normal muscle ROI and that of the prostate. Mean SNR and CNR values were calculated over all experiments.

Texture analysis was performed using a surface area metric (46), defined as the ratio of the 3D surface area (*SA*) of the plot of signal intensity vs. 'xy' position to its 2D projection area (*A*) onto the 'xy' plane (equation 1):

$$\frac{SA}{A}=\frac{\sum\sqrt{1+(\partial I/\partial x)^2+(\partial I/\partial y)^2}}{number\ of\ pixels} \quad \text{Eq. [1]}$$

where *I* is the image intensity at pixel (*x*, *y*). Texture was calculated over the manually segmented prostate. IDL was used to determine partial derivatives, which were computed numerically with a 3-point, Lagrangian interpolation method.

An estimate in the change in size of the prostate as a function of age was calculated from the cross-sectional area of the segmented prostate ROI for each experiment. An average ROI size was calculated for younger and older mice (less than and greater than 34 weeks, respectively). This produced two groups of mice with a difference of approximately six weeks between mean ages.

Histology

After the final imaging experiment, each mouse was sacrificed and its urogenital tract was resected. The excised tissue was preserved and stored in formalin and sent to pathology for histological slide preparation. Tissue samples were H & E stained for cancerous cell identification and slides were qualitatively compared with images.

RESULTS

Deuterated Catheter

Figure 1 shows the results of HiSS imaging with and without the insertion of the partially deuterated water filled catheter inserted in the mouse rectum for magnetic susceptibility matching. Without the catheter (Fig. 1a), the region about the colon shows a significant decrease in signal that is not present when the catheter is inserted (Figure 1b). The effect of matching the susceptibility in the colon with the surrounding tissue minimizes signal loss and prevents potential occlusion of the prostate.

Histology

The prostate appears normal at 29 weeks whereas hyperplasia/prostatic intraepithelial neoplasm (PIN), a precursor to prostate adenocarcinoma, is predominant at 37 weeks. Figure 2 shows representative histological slides of the prostate from mice at (a) 29 weeks and (b) 37 weeks. Figures 2a and 2b were cut sagittaly and axially, respectively, through the

resected urogenital tract. PIN in older mice can be seen as clusters of lobular structures (tubuloalveolar glands) approximately 200 microns to 400 microns in diameter.

Water peak height images display small lobular features in the prostate with sizes on the order of the individual tubuloalveolar glands (~200-400μm) in Figure 2. These structures appear only within the prostate and were found more frequently in older mice (Figure 3b-c) than in younger (figure 3a). These features were not discernible in gradient echo and spin echo images (Figure 4).

Imaging Metrics

Mean CNR and SNR values for the pooled data from all experiments are reported in Figure 5, independent of age. The mean CNR was greatest in the water peak height images ($p < 0.03$, paired two-tailed Student's t-test). Despite the fact that HiSS images were acquired at high spectral resolution, the signal-to-noise ratio compared favorably to that of the 'collapsed' images and conventional images. In fact, under the conditions of these experiments, the mean SNR was greater than those of the three other image types ($p < 0.002$, paired two-tailed Student's t-test). Visual inspection of the water peak height image suggests that it shows greater morphological detail than the corresponding gradient echo and spin echo images and the boundaries of the prostate are more clearly delineated.

A mean texture metric over all pooled experimental data of 4.48 ± 1.76 was calculated for the prostate in water peak height images, compared with 1.12 ± 0.08, 2.58 ± 0.99 and 1.87 ± 0.60 for the 'collapsed', gradient echo, and spin echo images, respectively. This difference was statistically significant ($p < 0.004$, paired two-tailed Student's t-test). Texture was inversely related to age; the correlation coefficients, R, were -0.77, -0.86, and -0.68 for water peak height, gradient echo and spin echo images vs. age. This was not found to be the case with the 'collapsed' image ($R = 0.02$).

Water peak height images show increased prostate size in mice over 34 weeks of age (mean ROI size = 25.02 ± 10.57 mm^2) compared to mice less than 34 weeks of age (mean ROI size = 13.55 ± 2.46 mm^2). This difference was statistically significant ($p < 0.1$ using a two-tailed unequal variance student t-test). The large standard deviation for the older mice is likely caused by poorly differentiated boundaries of the prostate. This reduces the statistical significance of this comparison with such small sample populations.

Discussion

Texture and contrast-to-noise ratio were greater in the water peak height images compared with gradient echo and spin echo images. Improvement in detection of morphological heterogeneity could lead to improved tissue differentiation and earlier detection of cancer. The results obtained here with HiSS MRI are consistent with previously reported in studies of implanted rodent tumors and human breast (17).

High spectral resolution was required to obtain the improvements in contrast and texture. Despite, this requirement, the signal-to-noise ratio of the HiSS images compared very favorably to that of conventional images. In fact, in the present experiments, signal-to-noise

ratio of HiSS images was greater than that of conventional images. However, this comparison was performed simply to test whether HiSS images had adequate signal-to-noise ratio, and is not meant to suggest an intrinsic signal-to-noise ratio advantage of HiSS.

Mean prostate ROI sizes indicate that the prostate grows significantly over many weeks; this result is in agreement with Fricke *et al* (39). The population size for each age group is small, so these results represent a preliminary finding that will require further investigation. In the present research only a single slice was scanned with HiSS in each prostate. An effort was made to ensure that the area of the prostate measured in each experiment came from approximately the same anatomical location in each mouse. This would minimize differences in prostate area associated with varying anatomical positions, but that is a potential source of error in our measurement. In future work 3D EPSI will be used to acquire HiSS data of the entire prostate so that the prostate volume can be determined.

Lobular structures, similar in size and shape to hyperplastic, tubuloalveolar glands seen on histology, are visible in HiSS prostate images. These structures were detected with increasing frequency in older mice (Figure 3). They have a relatively smooth appearance on MRI, and could be responsible for the observed decrease in image texture with age. These are qualitative observations, based on a small sample, and will require verification in a more extensive study with quantitative image analysis to objectively identify the lobules. Comparisons with other imaging techniques – such as fast spin echo methods, and diffusion-weighted imaging - will also be necessary to further evaluate the potential advantages of images derived from HiSS datasets. However, the qualitative results suggest the possibility of using HiSS to detect very early prostatic changes associated with increased cancer risk, as well as early cancers.

Microscopic variations in magnetic susceptibility are a critical source of contrast in HiSS images. In order to detect these local susceptibility variations, macroscopic magnetic field gradients must be minimized. Discontinuous changes, such as tissue/air interfaces, have the effect of broadening the waterline and decreasing the water peak height; as is evident by the blooming artifact found in the colon of mice. The partially deuterated water filled catheter is a useful technique for overcoming this problem.

The HiSS images discussed here were produced from the peak amplitude of the water resonance in each image voxel. However, the detailed water spectrum associated with each image voxel provides other features that may have diagnostic utility. For example, Fourier components of the water resonance that lie away from the main water peak are a possible source of novel, clinically useful contrast (29). Shoulders and partially resolved Fourier components of the water line may be caused by deoxygenated blood in tumor neo-vasculature (47,48), and thus may improve tumor vasculature detection.

In the present experiments, TR was determined by a slightly fluctuating respiration rate due to respiratory gating. This may have reduced image quality. In future studies intubation of the mice is planned so that a constant respiration rate can be maintained.

A number of other promising methods are currently being used or developed for prostate imaging. These include, for example, T_1, T_2, and diffusion-weighted imaging. The present

results suggest that HiSS MRI is a useful additional option and may provide complimentary information. An attractive feature of HiSS imaging is that it can be combined with other methods; for example, spin echo images can also be acquired with high spectral resolution.

Conclusion

We have demonstrated that, compared with conventional MRI, HiSS water peak height images of prostate have improved anatomical morphology and signal-to-noise and contrast-to-noise ratios. This is consistent with previous findings. Lobular structures are detected on HiSS images that are consistent with prostate hyperplasia and tubuloalveolar gland distension. However, more quantitative analysis of these features in a larger number of prostates is required. These results were obtained in a realistic model of human prostate cancer. Unlike previous MRI studies of murine prostate cancer, the present research focused on MRI of normal prostate and early hyperplastic changes. HiSS scans can be acquired with reasonable run times in humans. Therefore, the results reported here have implications for clinical MRI of the prostate.

Acknowledgments

This work was funded by the NCI (4R33CA100996-02) and NIBIB (5RO1EB003108-03). SF would also like to thank the Paul C. Hodges Alumni Society for the generous startup grant that supported this work.

References

1. American Cancer Society. Cancer Facts & Figures 2007. Atlanta, GA: American Cancer Society; 2007.
2. Prostate-specific antigen (PSA) best practice policy. American Urological Association (AUA). Oncology (Williston Park). 2000; 14(2):267–272. 277–268. 280 passim. [PubMed: 10736812]
3. Walsh PC. Screening for prostate cancer: recommendation and rationale. J Urol. 2003; 170(1):313.
4. Gohagan JK, Prorok PC, Hayes RB, Kramer BS. The Prostate, Lung, Colorectal and Ovarian (PLCO) Cancer Screening Trial of the National Cancer Institute: history, organization, and status. Control Clin Trials. 2000; 21(6 Suppl):251S–272S. [PubMed: 11189683]
5. de Koning HJ, Auvinen A, Berenguer Sanchez A, Calais da Silva F, Ciatto S, Denis L, Gohagan JK, Hakama M, Hugosson J, Kranse R, Nelen V, Prorok PC, Schroder FH. Large-scale randomized prostate cancer screening trials: program performances in the European Randomized Screening for Prostate Cancer trial and the Prostate, Lung, Colorectal and Ovary cancer trial. Int J Cancer. 2002; 97(2):237–244. [PubMed: 11774270]
6. Ryan CJ, Small EJ. Prostate cancer update: 2005. Curr Opin Oncol. 2006; 18(3):284–288. [PubMed: 16552242]
7. Ross R, Harisinghani M. New clinical imaging modalities in prostate cancer. Hematol Oncol Clin North Am. 2006; 20(4):811–830. [PubMed: 16861116]
8. Sanchez-Chapado M, Angulo JC, Ibarburen C, Aguado F, Ruiz A, Viano J, Garcia-Segura JM, Gonzalez-Esteban J, Rodriquez-Vallejo JM. Comparison of digital rectal examination, transrectal ultrasonography, and multicoil magnetic resonance imaging for preoperative evaluation of prostate cancer. Eur Urol. 1997; 32(2):140–149. [PubMed: 9286643]
9. Beyersdorff D, Hamm B. MRI for troubleshooting detection of prostate cancer. Rofo. 2005; 177(6): 788–795. [PubMed: 15902626]
10. Grossfeld GD, Coakley FV. Benign prostatic hyperplasia: clinical overview and value of diagnostic imaging. Radiol Clin North Am. 2000; 38(1):31–47. [PubMed: 10664665]

11. Poon PY, McCallum RW, Henkelman MM, Bronskill MJ, Sutcliffe SB, Jewett MA, Rider WD, Bruce AW. Magnetic resonance imaging of the prostate. Radiology. 1985; 154(1):143–149. [PubMed: 2578070]
12. Ling D, Lee JK, Heiken JP, Balfe DM, Glazer HS, McClennan BL. Prostatic carcinoma and benign prostatic hyperplasia: inability of MR imaging to distinguish between the two diseases. Radiology. 1986; 158(1):103–107. [PubMed: 2416005]
13. Okamura T, Umemoto Y, Yamashita K, Suzuki S, Shirai T, Hashimoto Y, Kohri K. Pitfalls with MRI evaluation of prostate cancer detection: comparison of findings with histopathological assessment of retropubic radical prostatectomy specimens. Urol Int. 2006; 77(4):301–306. [PubMed: 17135778]
14. Adusumilli S, Pretorius ES. Magnetic resonance imaging of prostate cancer. Semin Urol Oncol. 2002; 20(3):192–210. [PubMed: 12215973]
15. Brassell SA, Krueger WR, Choi JH, Taylor JA 3rd. Correlation of endorectal coil magnetic resonance imaging of the prostate with pathologic stage. World J Urol. 2004; 22(4):289–292. [PubMed: 15365749]
16. Costouros NG, Coakley FV, Westphalen AC, Qayyum A, Yeh BM, Joe BN, Kurhanewicz J. Diagnosis of prostate cancer in patients with an elevated prostate-specific antigen level: role of endorectal MRI and MR spectroscopic imaging. AJR Am J Roentgenol. 2007; 188(3):812–816. [PubMed: 17312072]
17. Kovar DA, Al-Hallaq HA, Zamora MA, River JN, Karczmar GS. Fast spectroscopic imaging of water and fat resonances to improve the quality of MR images. Acad Radiol. 1998; 5(4):269–275. [PubMed: 9561260]
18. Karczmar GS, Fan X, Al-Hallaq H, River JN, Tarlo K, Kellar KE, Zamora M, Rinker-Schaeffer C, Lipton MJ. Functional and anatomic imaging of tumor vasculature: high-resolution MR spectroscopic imaging combined with a superparamagnetic contrast agent. Acad Radiol. 2002; 9(Suppl 1):S115–118. [PubMed: 12019844]
19. Du W, Du YP, Bick U, Fan X, MacEneaney PM, Zamora MA, Medved M, Karczmar GS. Breast MR imaging with high spectral and spatial resolutions: preliminary experience. Radiology. 2002; 224(2):577–585. [PubMed: 12147859]
20. Mansfield P. Spatial mapping of the chemical shift in NMR. Magn Reson Med. 1984; 1(3):370–386. [PubMed: 6571566]
21. Mansfield P. Real-time echo-planar imaging by NMR. Br Med Bull. 1984; 40(2):187–190. [PubMed: 6744006]
22. Chu SC, Xu Y, Balschi JA, Springer CS Jr. Bulk magnetic susceptibility shifts in NMR studies of compartmentalized samples: use of paramagnetic reagents. Magnetic resonance in medicine : official journal of the Society of Magnetic Resonance in Medicine / Society of Magnetic Resonance in Medicine. 1990; 13(2):239–262.
23. Yablonskiy DA, Haacke EM. Theory of NMR signal behavior in magnetically inhomogeneous tissues: the static dephasing regime. Magn Reson Med. 1994; 32(6):749–763. [PubMed: 7869897]
24. Sukstanskii AL, Yablonskiy DA. Theory of FID NMR signal dephasing induced by mesoscopic magnetic field inhomogeneities in biological systems. J Magn Reson. 2001; 151(1):107–117. [PubMed: 11444944]
25. Spees WM, Yablonskiy DA, Oswood MC, Ackerman JJ. Water proton MR properties of human blood at 1.5 Tesla: magnetic susceptibility, T(1), T(2), T*(2), and non-Lorentzian signal behavior. Magn Reson Med. 2001; 45(4):533–542. [PubMed: 11283978]
26. Reichenbach JR, Venkatesan R, Schillinger DJ, Kido DK, Haacke EM. Small vessels in the human brain: MR venography with deoxyhemoglobin as an intrinsic contrast agent. Radiology. 1997; 204(1):272–277. [PubMed: 9205259]
27. Karczmar GS, Du W, Medved M, Bick U, MacEneany P, Du YP, Fan X, Zamora M, Lipton M. Spectrally inhomogeneous effects of contrast agents in breast lesion detected by high spectral and spatial resolution MRI. Acad Radiol. 2002; 9(Suppl 2):S352–354. [PubMed: 12188272]
28. Al-Hallaq HA, Fan X, Zamora M, River JN, Moulder JE, Karczmar GS. Spectrally inhomogeneous BOLD contrast changes detected in rodent tumors with high spectral and spatial resolution MRI. NMR Biomed. 2002; 15(1):28–36. [PubMed: 11840550]

29. Medved M, Newstead GM, Fan X, Du W, Du YP, MacEneaney PM, Culp RM, Kelcz F, Olopade OI, Zamora MA, Karczmar GS. Fourier components of inhomogeneously broadened water resonances in breast: a new source of MRI contrast. Magnetic resonance in medicine : official journal of the Society of Magnetic Resonance in Medicine / Society of Magnetic Resonance in Medicine. 2004; 52(1):193–196.
30. Babcock EE, Brateman L, Weinreb JC, Horner SD, Nunnally RL. Edge artifacts in MR images: chemical shift effect. J Comput Assist Tomogr. 1985; 9(2):252–257. [PubMed: 3973146]
31. Yang QX, Demeure RJ, Dardzinski BJ, Arnold BW, Smith MB. Multiple echo frequency-domain image contrast: improved signal-to-noise ratio and T2 (T2*) weighting. Magn Reson Med. 1999; 41(2):423–428. [PubMed: 10080294]
32. Du W, Fan X, Foxley S, Zamora M, River JN, Culp RM, Karczmar GS. Comparison of high-resolution echo-planar spectroscopic imaging with conventional MR imaging of prostate tumors in mice. NMR in biomedicine. 2005; 18(5):285–292. [PubMed: 15973657]
33. Du W, Karczmar GS, Uftring SJ, Du YP. Anatomical and functional brain imaging using high-resolution echo-planar spectroscopic imaging at 1.5 Tesla. NMR Biomed. 2005; 18(4):235–241. [PubMed: 15759296]
34. Fan X, Du W, MacEneaney P, Zamora M, Karczmar G. Structure of the water resonance in small voxels in rat brain detected with high spectral and spatial resolution MRI. Journal of magnetic resonance imaging : JMRI. 2002; 16(5):547–552. [PubMed: 12412031]
35. Medved M, Du W, Zamora MA, Fan X, Olopade OI, MacEneaney PM, Newstead G, Karczmar GS. The effect of varying spectral resolution on the quality of high spectral and spatial resolution magnetic resonance images of the breast. Journal of magnetic resonance imaging : JMRI. 2003; 18(4):442–448. [PubMed: 14508781]
36. Fan X, Abe H, Medved M, Foxley S, Arkani S, Zamora MA, Olopade OI, Newstead GM, Karczmar GS. Fat suppression with spectrally selective inversion vs. high spectral and spatial resolution MRI of breast lesions: qualitative and quantitative comparisons. Journal of magnetic resonance imaging : JMRI. 2006; 24(6):1311–1315. [PubMed: 17096393]
37. Hsu CX, Ross BD, Chrisp CE, Derrow SZ, Charles LG, Pienta KJ, Greenberg NM, Zeng Z, Sanda MG. Longitudinal cohort analysis of lethal prostate cancer progression in transgenic mice. J Urol. 1998; 160(4):1500–1505. [PubMed: 9751403]
38. Song SK, Qu Z, Garabedian EM, Gordon JI, Milbrandt J, Ackerman JJ. Improved magnetic resonance imaging detection of prostate cancer in a transgenic mouse model. Cancer Res. 2002; 62(5):1555–1558. [PubMed: 11888935]
39. Fricke ST, Rodriguez O, Vanmeter J, Dettin LE, Casimiro M, Chien CD, Newell T, Johnson K, Ileva L, Ojeifo J, Johnson MD, Albanese C. In vivo magnetic resonance volumetric and spectroscopic analysis of mouse prostate cancer models. Prostate. 2006; 66(7):708–717. [PubMed: 16425198]
40. Degrassi A, Russo M, Scanziani E, Giusti A, Ceruti R, Texido G, Pesenti E. Magnetic resonance imaging and histopathological characterization of prostate tumors in TRAMP mice as model for pre-clinical trials. Prostate. 2007; 67(4):396–404. [PubMed: 17187397]
41. Maroulakou IG, Anver M, Garrett L, Green JE. Prostate and mammary adenocarcinoma in transgenic mice carrying a rat C3(1) simian virus 40 large tumor antigen fusion gene. Proc Natl Acad Sci U S A. 1994; 91(23):11236–11240. [PubMed: 7972041]
42. Gleason, DF. The Veterans Administration Cooperative Urological Research Group. In: Tannenbaum, M., editor. Histologic grading and clinical staging of prostatic caricnoma. Philadelphia: Lea & Febiger; 1977.
43. Gruetter R. Automatic, localized in vivo adjustment of all first- and second-order shim coils. Magn Reson Med. 1993; 29(6):804–811. [PubMed: 8350724]
44. Du W, Du YP, Fan X, Zamora MA, Karczmar GS. Reduction of spectral ghost artifacts in high-resolution echo-planar spectroscopic imaging of water and fat resonances. Magn Reson Med. 2003; 49(6):1113–1120. [PubMed: 12768590]
45. Cho ZH, Nalcioglu O, Park HW, Ra JB, Hilal SK. Chemical-shift artifact correction scheme using echo-time encoding technique. Magn Reson Med. 1985; 2(3):253–261. [PubMed: 3831694]

46. Fan X, River JN, Zamora M, Tarlo K, Kellar K, Rinker-Schaeffer C, Karczmar GS. Differentiation of nonmetastatic and metastatic rodent prostate tumors with high spectral and spatial resolution MRI. Magn Reson Med. 2001; 45(6):1046–1055. [PubMed: 11378883]

47. Foxley, S.; Yang, C.; Fan, X.; Zamora, M.; Panti, R.; River, JN.; Karczmar, G. Increased sensitivity to tumor oxygenation in mice using high resolution echo-planar spectroscopic imaging. South Beach, Miami, FL: 2005.

48. Foxley, S.; Yang, C.; Fan, X.; Zamora, M.; Panti, R.; River, JN.; Karczmar, G. The use of high spatial and spectral resolution Fourier component difference images to detect BOLD response in mouse tumors. South Beach, Miami, FL: 2005.

Abbreviations

PSA	Prostate specific antigen
EPSI	Echo-planar spectroscopic imaging
HiSS	High spectral and spatial resolution imaging
SNR	Signal-to-noise ratio
CNR	Contrast-to-noise ratio
FOV	Field of view
NEX	Number of averages
PIN	Prostatic intraepithelial neoplasia
PH	Peak height
GE	Gradient echo
SE	Spin echo

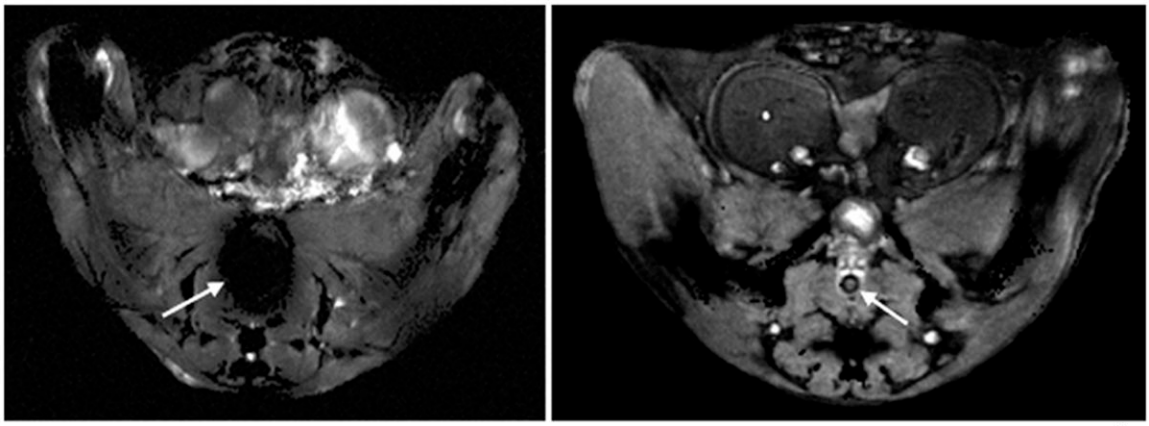

a. b.

Figure 1.

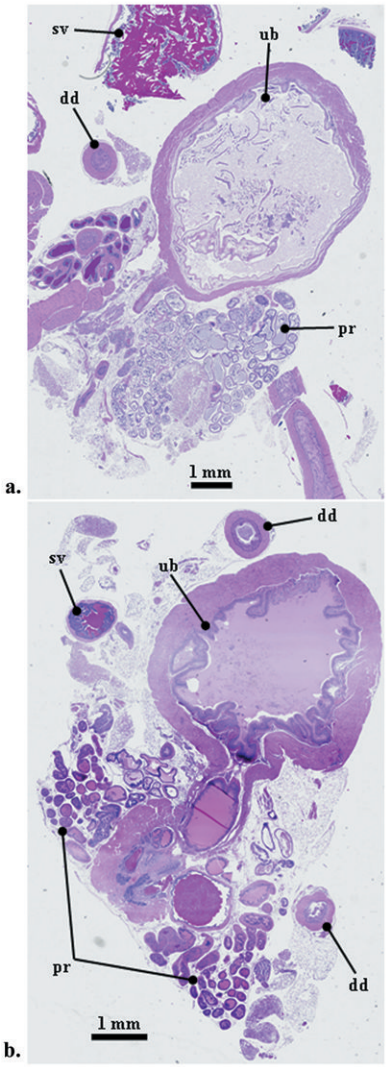

Figure 2.

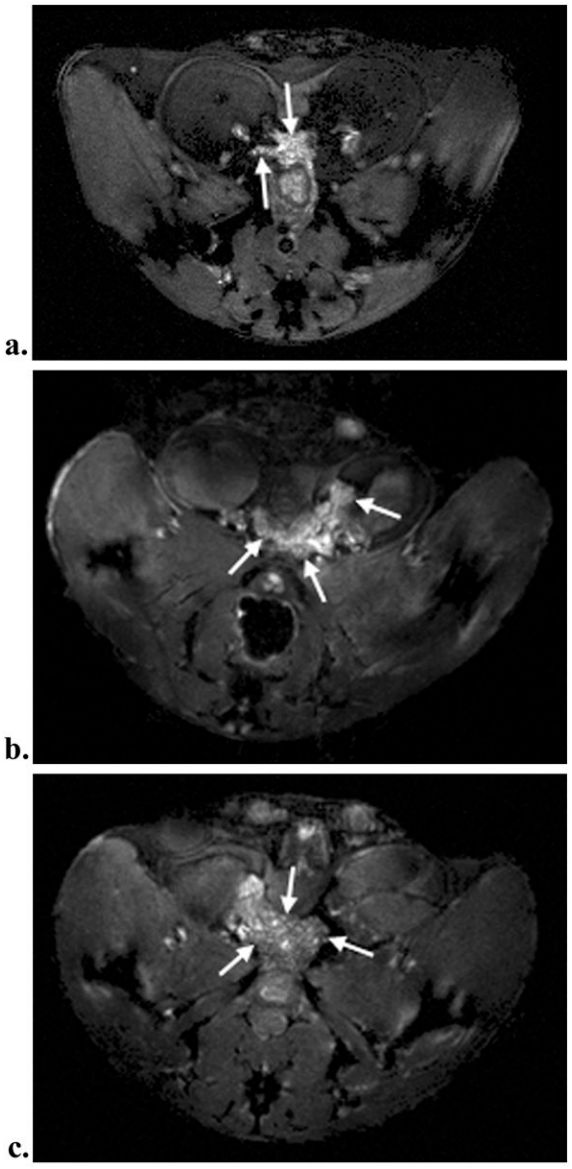

Figure 3.

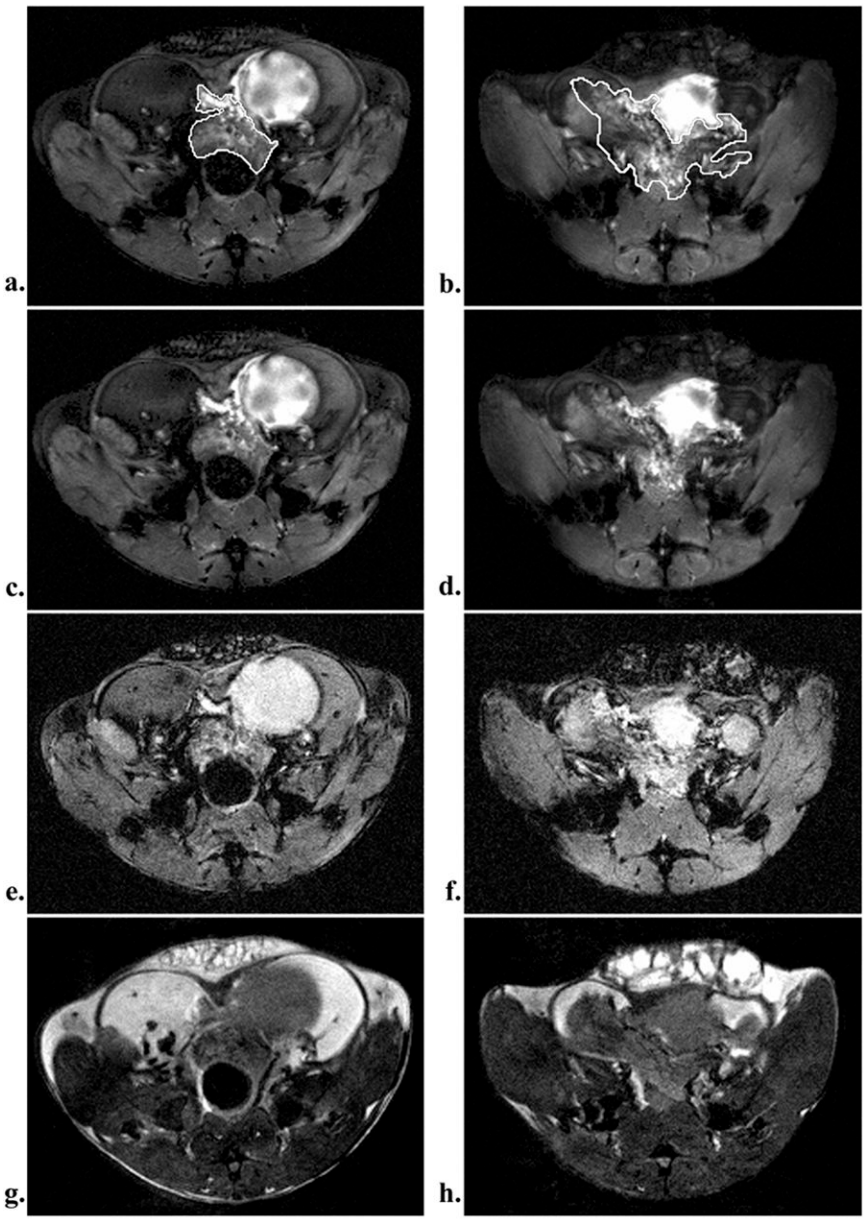

Figure 4.

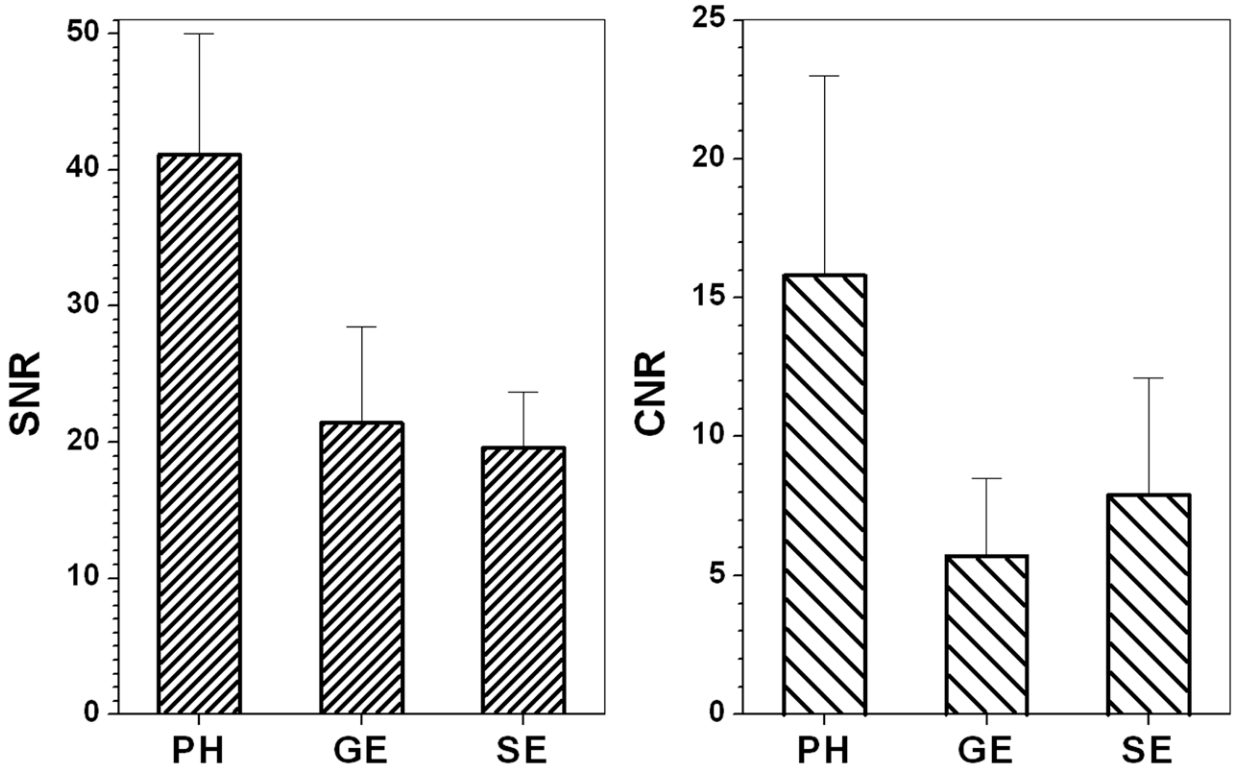

Figure 5.